3-D acoustic-elastic full-waveform inversion and migration of marine VSP data from Norway

Zhaolun Liu[*1], Jürgen Hoffmann[2], Frederik J. Simons[1], and Jeroen Tromp[1]*
[1]*Princeton University*, [2]*DNO ASA*

Summary

We demonstrate an application of three-dimensional (3-D) acoustic-elastic coupled Full-Waveform Inversion (FWI) to deviated Rig-source Vertical Seismic Profile (R-VSP) data from the Fenja Field in Norway, to advance our understanding of subsurface structure. We perform 3-D Reverse-Time Migration (RTM) of the data using the inverted wave speed models. The RTM results show that the structures in our 3-D compressional speed (V_P) image are a better match with those obtained from surface seismic imaging, compared to the legacy 2-D ray-based migration image. The resolution of our shear wave speed (V_S) image is higher than that of the V_P image due to the smaller reflection angle of P-to-S converted waves compared to that of P-to-P reflections. Our V_S and density (ρ) images yield additional structural information.

Introduction

The R-VSP survey was recorded in a deviated well of the Fenja field, Norway, with 163 receivers recording the data. Of those, 109 recorded between 4233–1236 m MD (Measured Depth) at 27.8 m spacing, and 54 receivers recorded between 5011–4261 m MD with 13.9 m spacing. Data collected in the interval 2568–1236 m MD were affected by casing noise and removed from processing. At each receiver, a hydrophone and three orthogonal geophones recorded four-component (4-C) data. In our study, we used only the three-component (3-C) geophone data, after 3-D rotation to the geographic orientation.

The initial processing of the R-VSP data is based on a 2-D time-domain ray-based migration method (Miller et al., 1987). The complex well trajectory (Fig. 1) as well as the 3-D target geometry suggest that the 2-D assumption may not be adequate. Additionally, P-to-S converted waves in the RVSP data may contain valuable information and currently are not used, which entails the loss of subsurface structure information. This motivated us to apply more accurate seismic modeling and imaging methods to this data set. Here, we used a 3-D acoustic-elastic coupled forward modeling method to simulate the 3-C data and apply 3-D acoustic-elastic coupled FWI and RTM (Luo et al., 2013; Cao et al., 2021) to improve the accuracy of the model parameters and the migration images.

We built 3-D initial S-wave speed (V_S) and density (ρ) models from the legacy 3-D P-wave speed (V_P) models, based on the 1-D V_P/V_S ratio estimated from sonic logs. The 3-C synthetic seismic data were generated using SPECFEM3-D (Komatitsch and Tromp, 1999), which can simulate a 3-D acoustic-elastic coupled system and account for elastic effects like P-to-S conversions on the solid seabed. Next, we applied 3-D FWI methods on the deviated R-VSP data. Afterward, the 3-D RTM method was used to image the subsurface structure. Finally, we compared our 3-D RTM images with the available legacy 2-D migration images, and with images from surface seismic data.

Theory

We first introduce the acoustic-elastic coupled wave-equation system implemented in SPECFEM3-D. In the acoustic (Ω_{ac}) and elastic (Ω_{el}) domains, the system of wave equations is

$$\rho \partial_t^2 \mathbf{s} = \nabla \cdot (\mathbf{c} : \nabla \mathbf{s}) \qquad \text{in } \Omega_{el}, \qquad (1)$$

$$\kappa^{-1} \partial_t^2 \phi = \nabla \cdot (\rho^{-1} \nabla \phi) + f \qquad \text{in } \Omega_{ac}, \qquad (2)$$

$$\partial_t^2 \phi = 0 \qquad \text{on } \partial\Omega, \qquad (3)$$

$$\rho^{-1} \hat{\mathbf{n}} \cdot \nabla \phi = \hat{\mathbf{n}} \cdot \mathbf{s}, \quad -p\hat{\mathbf{n}} = \hat{\mathbf{n}} \cdot (\mathbf{c} : \nabla \mathbf{s}) \ \text{ on } \Gamma, \qquad (4)$$

where $\mathbf{s}(\mathbf{x},t)$ is displacement, ρ mass density, $\mathbf{c}$ the stiffness tensor, and κ denotes the bulk modulus. A scalar potential ϕ is defined in the acoustic domain Ω_{ac} such that $\mathbf{s} = \rho^{-1}\nabla\phi$. It follows that pressure p may be expressed as,

$$p = -\kappa(\nabla \cdot \mathbf{s}) = -\partial_t^2 \phi. \qquad (5)$$

The source f may be expressed in terms of the pressure P_f acting at location $\mathbf{x}_s$ for a marine R-VSP survey,

$$f(t) = -\kappa^{-1} P_f(t) \delta(\mathbf{x} - \mathbf{x}_s). \qquad (6)$$

At the free surface $\partial\Omega$, we set the pressure $p = -\partial_t^2\phi = 0$. On the boundary between the elastic and acoustic domains Γ, the normal component of the displacement $\hat{\mathbf{n}} \cdot \mathbf{s}$ and the traction $\hat{\mathbf{n}} \cdot (\mathbf{c} : \nabla \mathbf{s})$ are continuous.

The misfit of FWI applied to the R-VSP data can be written as (Tromp et al., 2005),

$$\chi(\mathbf{m}) = \sum_{r=1}^{N_r} \int_0^T \frac{1}{2} ||\mathbf{s}(\mathbf{x}_r,t;\mathbf{m}) - \mathbf{d}(\mathbf{x}_r,t)||^2 dt, \qquad (7)$$

where $\mathbf{d}(\mathbf{x}_r,t)$ represents observed multi-component waveform data at receivers $\mathbf{x}_r$, $r = 1, \ldots, N_r$, and with $\mathbf{s}(\mathbf{x}_r,t;\mathbf{m})$ the corresponding synthetic data, computed in model $\mathbf{m}$. The gradient of the misfit function in eq. (7) can be obtained through the adjoint-state method (Plessix, 2006). The adjoint wave equations in the acoustic and elastic domain can be expressed as

$$\rho \partial_t^2 \mathbf{s}^\dagger = \nabla \cdot (\mathbf{c} : \nabla \mathbf{s}^\dagger) + \mathbf{f}^\dagger \qquad \text{in } \Omega_{el}, \qquad (8)$$

$$\kappa^{-1} \partial_t^2 \phi^\dagger = \nabla \cdot (\rho^{-1} \nabla \phi^\dagger) \qquad \text{in } \Omega_{ac}, \qquad (9)$$

$$\phi^\dagger = 0 \qquad \text{on } \partial\Omega, \qquad (10)$$

$$-\rho^{-1} \hat{\mathbf{n}} \cdot \nabla \phi^\dagger = \hat{\mathbf{n}} \cdot \partial_t^2 \mathbf{s}^\dagger, \quad -\phi^\dagger \hat{\mathbf{n}} = \hat{\mathbf{n}} \cdot (\mathbf{c} : \nabla \mathbf{s}^\dagger) \ \text{ on } \Gamma, \qquad (11)$$

where the adjoint source $\mathbf{f}^\dagger$ is located in the elastic domain,

$$\mathbf{f}^\dagger(\mathbf{x},t) = \sum_{r=1}^{N_r} [\mathbf{s}(\mathbf{x}_r,T-t) - \mathbf{d}(\mathbf{x}_r,T-t)] \delta(\mathbf{x} - \mathbf{x}_r). \qquad (12)$$

3-D elastic FWI of marine VSP data

The boundary conditions for adjoint wave equations at Γ in eq. 8 differ from those of the forward wave-equations in eq. 1. For more details, see Luo et al. (2013).

The misfit function in eq. (7) is very sensitive to amplitude errors in the data. In practice, we use a normalized cross-correlation misfit function (Sen and Stoffa, 1990; Choi and Alkhalifah, 2012),

$$\tilde{\chi}(\mathbf{m}) = -\sum_{j=1}^{N_r} \tilde{\mathbf{s}}_j \cdot \tilde{\mathbf{d}}_j, \tag{13}$$

where $\tilde{\mathbf{d}}_j = \mathbf{d}_j/||\mathbf{d}_j||$, $\mathbf{d}_j$ and $\mathbf{s}_j$ are the observed and synthetic trace vectors at receivers $\mathbf{x}_j$. The optimal model parameters m_l are obtained by gradient-update methods. For example, the steepest-descent formula is

$$m_l^{(k+1)} = m_l^{(k)} - \alpha \frac{\partial \tilde{\chi}(\mathbf{m})}{\partial m_l}, \tag{14}$$

where α is a step length, and the parenthetical superscript (k) denotes the kth iteration. In practice, the L-BFGS method is used for faster convergence (Nocedal and Wright, 2006). The elastic FWI workflow is carried out by SeisFlows (Modrak et al., 2018), a Python-based open-source package.

Numerical Results

The initial 3-D V_P model is shown in Fig. 2a. We estimated the V_P/V_S ratio from the sonic logs, and used it to calculate the 3-D V_S model shown in Fig. 2b from the initial 3-D V_P model. The initial ρ model is estimated from V_P by Gardner's relation,

$$\rho = 0.31 V_P^{0.25}. \tag{15}$$

We use the near-field pressure signature as the source-time function (STF) in our forward modeling (Fig. 3a). The measurement shows how the released air produces a steep-fronted shock wave followed by several oscillations that result from the repeated collapse and expansion of the air bubble (Sheriff and Geldart, 1995), with a period of 165 ms. Spectral analysis of the STF in Fig. 3b shows its minimum frequency is 7 Hz.

We use SPECFEM3-D to carry out forward modeling. The observed and synthetic vertical-component data are shown in Fig. 4a and 4b, respectively. The trace-by-trace comparison is given in Fig. 5, where the synthetic and observed data are in green and blue, respectively. Comparing the synthetic data with the observed data, we can see that our forward modeling method can simulate the *bubble effect* (dashed red lines in Fig. 4) and *seafloor multiples* (dashed yellow lines in Fig. 4). Those synthetic multiples match well with the observed ones (Fig. 4b). Transmitted *S*-waves show up in the synthetics (blue boxes in Fig. 4b) but not in the observations (Fig. 4a). We will mute out all the transmitted *S*-waves in the synthetic data in the following process. We can see that for the shallow receivers (numbered 1–55), both the waveforms and the traveltimes of the early arrivals and multiples match very well. There are some traveltime differences (less than half a period) for the

bottom receivers (numbered 56–114), which can be reduced by the following 3-D FWI.

3-D acoustic-elastic coupled FWI

We first apply 3-D acoustic-elastic coupled FWI to the early-arrival waveforms using a time window of 0.3 s, where 10 Hz low-pass filters are used for the observed and synthetic data during the inversion. We then update the STF by a linear inversion using the inverted models (Liu et al., 2021). Next, we reduce data muting with a time window of 1.7 s to perform FWI on the late arrivals, where a 10 Hz low-pass filter is applied. After that, we successively invert datasets of increasingly high-frequency content from 15 Hz to 30 Hz.

The synthetic vertical-component data calculated from the inverted models are shown Fig. 4c. The trace-by-trace comparison is given in Fig. 5, in red. Here, the gray and red numbers on the right-hand side of each panel are $100\times$ the cross-correlation coefficients between the observed and the synthetic data from the initial and inverted models, respectively (with maximum value 100). We bolded the numbers when the cross-correlation coefficient increased after inversion. We notice how the synthetic data match the observed data better after inversion. The average cross-correlation coefficients increased from 0.75 to 0.95 after FWI.

The V_P and V_S model updates are shown in Figs 6a and 6b, respectively. We see that most of the V_P updates are located between the source and receiver, while most V_S updates are close to the receiver sides. That is because the observed data lack direct *S*-waves, and only *P*-to-*S* converted waves are used for updating the V_S model. We see only approximately 5% and 3% wave speed updates for V_P and V_S models, respectively. The limited updates by FWI are due to the limited R-VSP data set with only one source location which illuminates only a small part of the subsurface.

3-D acoustic-elastic coupled RTM

We first extract the up-going waves from the data using the Hilbert transform (Wang et al., 2016). Fig. 8 shows the up-going waves separated from the 3-C 30 Hz data. The 3-C up-going waves are migrated by 3-D acoustic-elastic coupled RTM to obtain the 3-D VSP RTM V_P, V_S and ρ images, as shown in Figs 8d–8f, where a 3-D transparent white surface mutes out the migration artifacts. We then compare our results with the 2-D legacy migration images (yellow polygons in Figs 9a) and 3-D images from surface seismic data.

For comparison, we extract the 2-D image along the receiver trajectory from the 3-D surface seismic image cube (Fig. 7, background image in Fig. 9) and the 3-D VSP RTM images (yellow polygons in Figs 9b, 9c, and 9d). Here, we highlight some structures using the dashed red lines, dashed green circles, and numbered arrows which are prominent in the images from surface seismic data. From Fig. 9, we can see that there are common structures in the legacy VSP images, surface seismic images, and VSP RTM images, such as the structures indicated by arrows numbered 1, 2 and 4 in Fig. 9. The structures in the VSP RTM images match better with those in the surface seismic images, for example, the structures marked by the ar-

rows numbered 3 and 5 through 7 in Fig. 9. The prominent structures within the blue circles of Fig 9 in the RTM images also exist in the legacy V_P image, which is very weak in the surface seismic image.

We can see structural discontinuities in the legacy V_P image within the green dashed circles of Fig. 9a. However, we do not see those structures either in the VSP RTM images or in the surface seismic image. Those discontinuous structures marked by green circles in the legacy V_P images could be migration artifacts caused by the 2-D assumption and the use of the ray-based time-domain migration method. The resolution of the RTM V_S image is higher than that of the RTM V_P image due to the smaller reflection angle of P-to-S converted waves compared to that of P-to-P reflections. There is additional structural information in the RTM V_S images, for example, the structures marked by arrow numbered 8 in Fig. 9.

Conclusion

We applied 3-D acoustic-elastic coupled FWI and RTM to Rig source VSP data collected from a deviated well in the Fenja field in Norway. While the model updates by FWI are ultimately minor due to the limited number of shots and receivers, the structures in our 3-D RTM V_P image ($<$30 Hz) match better with those in the surface seismic images compared to the legacy migration image (7–80 Hz). The resolution of the VSP RTM V_S image is higher than that of the VSP RTM V_P image due to the smaller reflection angle of P-to-S converted waves compared to that of P-to-P reflections. There is additional structural information in the 3-D VSP RTM V_S and ρ images.
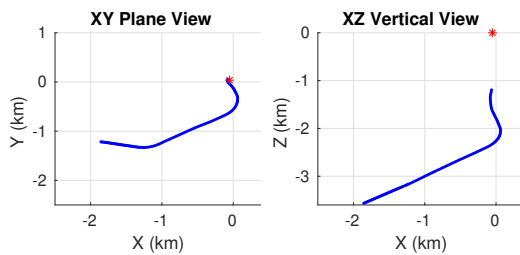
Acknowledgments

Figure 1: The deviated 3-D well geometry. The well is deviated with a maximum deviation of 59.72°. Here, the red and blue dots represent the locations of the source and receivers, respectively.
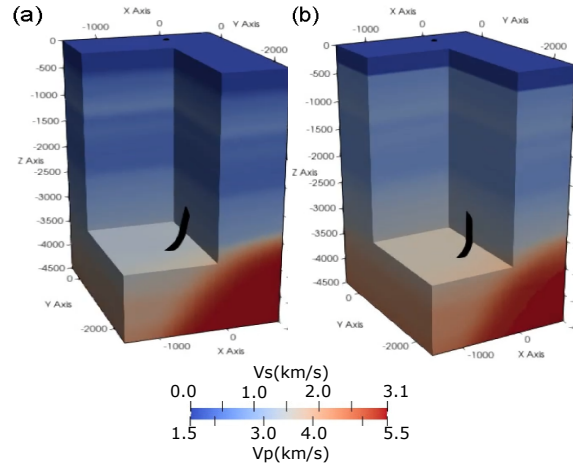

Figure 2: Initial (a) V_P and (b) V_S models used in the 3-D acoustic-elastic coupled modeling.
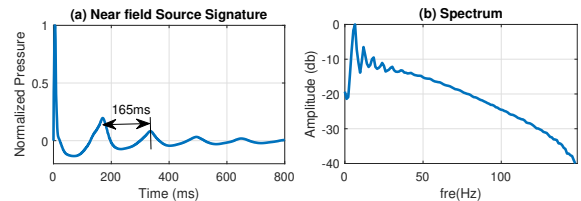

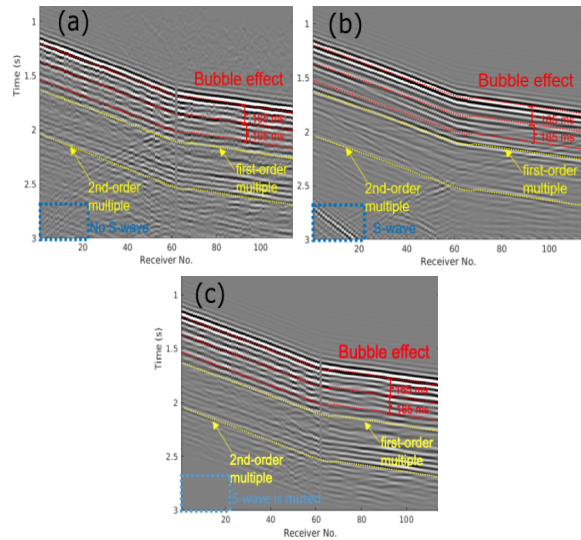Figure 3: (a) Source time function and (b) its spectrum.

Figure 4: (a) Observed and (b–c)synthetic vertical-component data calculated from the (b) initial and (c) inverted models. The red dashed lines indicate the seismic events due to bubble effects. The yellow lines indicate seafloor multiples. There are strong S-waves in the blue boxes of (b).
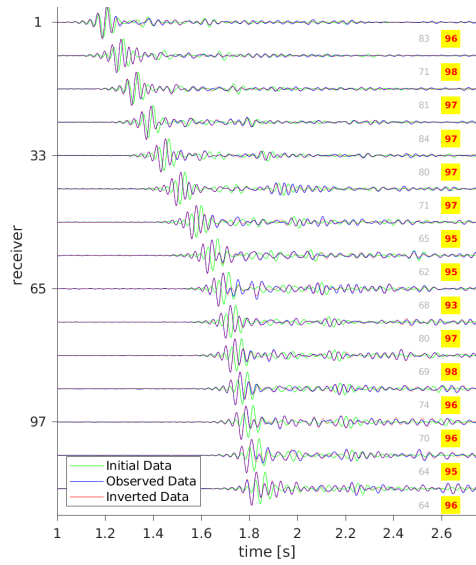
3-D elastic FWI of marine VSP data

Figure 5: Comparison of vertical-component observed data (blue) and synthetics calculated from the initial (green) and inverted (red) models. The gray and red numbers on the right-hand side for each trace are $100\times$ the cross-correlation co-efficients between the observed and the synthetic data from the initial and inverted model, respectively (maximum is 100). We highlight the number with a yellow background when the cross-correlation coefficient increases after inversion.
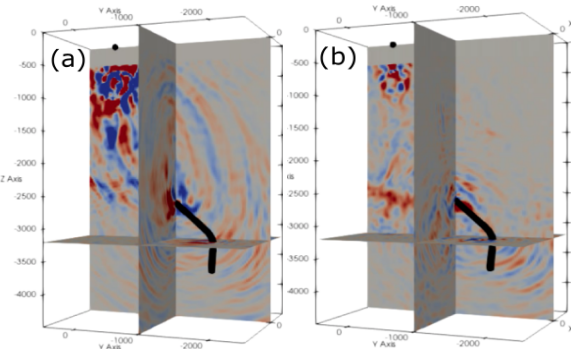

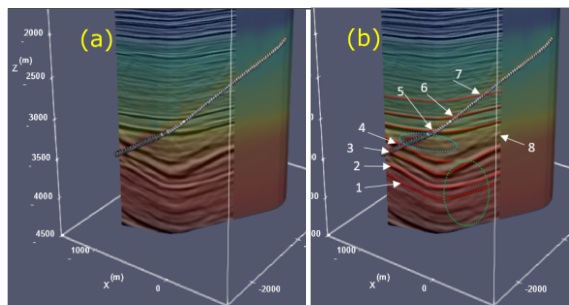Figure 6: (a) V_P and (b) V_S model updates by FWI.

Figure 7: (a) The extracted 2-D migration image along the re-ceiver trajectory from the 3-D surface seismic image. (b) Same as (a) but with annotation marks. (data courtesy of PGS)
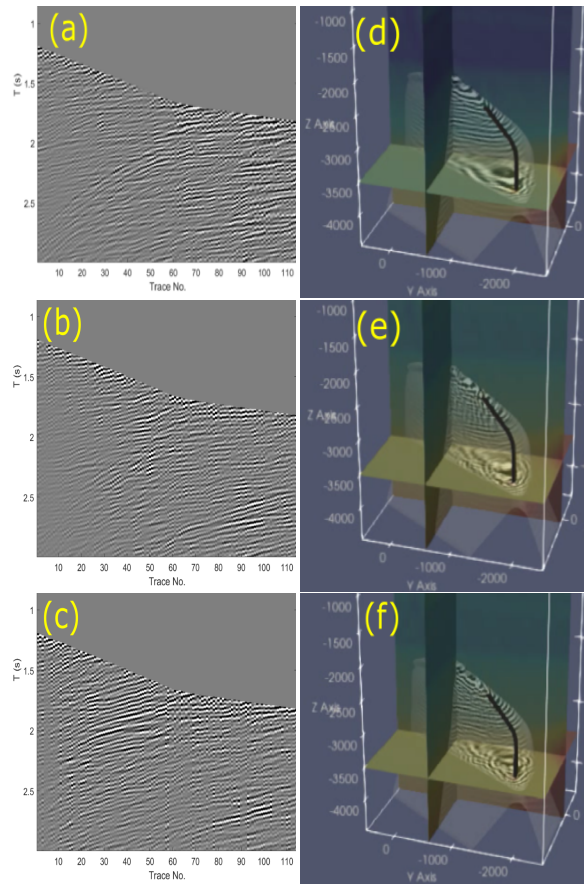

Figure 8: Up-going waves for the 30 Hz (a) z- (vertical), (b) x-, and (c) y-component data. 3-D (d) V_P, (e) V_S and (f) ρ images from RTM.
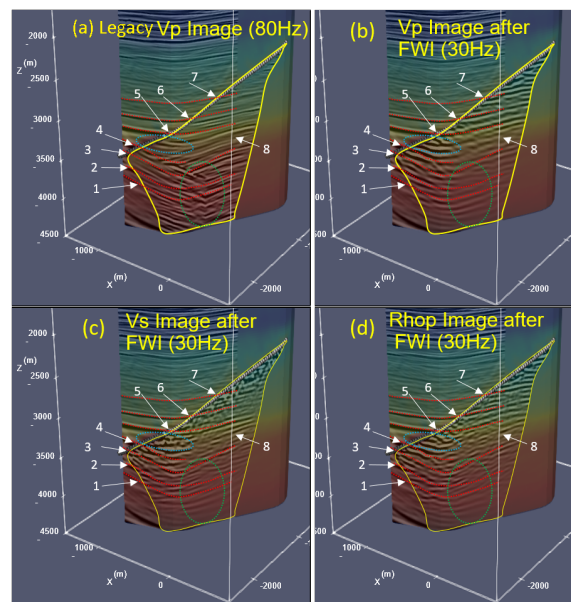

Figure 9: VSP images in yellow polygons are overlain on the background surface seismic image: (a) the legacy V_P image; (b) V_P, (c) V_S, and (d) ρ images from RTM.

REFERENCES

Cao, J., R. Brossier, and L. Metivier, 2021, 3D fluid-solid coupled full-waveform inversion for ocean-bottom seismic data: Presented at the First International Meeting for Applied Geoscience & Energy Expanded Abstracts, 832–836, doi:–https://doi.org/10.1190/segam2021–3583300.1.

Choi, Y., and T. Alkhalifah, 2012, Application of multi-source waveform inversion to marine streamer data using the global correlation norm: Geophysical Prospecting, **60**, 748–758, doi: –https://doi.org/10.1111/j.1365–2478.2012.01079.x.

Komatitsch, D., and J. Tromp, 1999, Introduction to the spectral element method for three-dimensional seismic wave propagation: Geophysical Journal International, **139**, 806–822.

Liu, Z., J. Hoffmann, F. J. Simons, and J. Tromp, 2021, Elastic full-waveform inversion of VSP data from a complex anticline in northern Iraq: Presented at the First International Meeting for Applied Geoscience & Energy Expanded Abstracts, 637–641, doi: –https://doi.org/10.1190/segam2021–3582871.1.

Luo, Y., J. Tromp, B. Denel, and H. Calandra, 2013, 3D coupled acoustic-elastic migration with topography and bathymetry based on spectral-element and adjoint methods: Geophysics, **78**, no. 4, S193–S202, doi: –https://doi.org/10.1190/geo2012–0462.1.

Miller, D., M. Oristaglio, and G. Beylkin, 1987, A new slant on seismic imaging: Migration and integral geometry: Geophysics, **52**, 943–964, doi: https://doi.org/10.1190/1.1442364.

Modrak, R. T., D. Borisov, M. Lefebvre, and J. Tromp, 2018, SeisFlows—Flexible waveform inversion software: Computers and Geosciences, **115**, 88–95, doi: https://doi.org/10.1016/j.cageo.2018.02.004.

Nocedal, J., and S. J. Wright, 2006, Numerical optimization: Springer, Operations Research and Financial Engineering.

Plessix, R.-E., 2006, A review of the adjoint-state method for computing the gradient of a functional with geophysical applications: Geophysical Journal International, **167**, 495–503, doi: –https://doi.org/10.1111/j.1365–246X.2006.02978.x.

Sen, M. K., and P. L. Stoffa, 1990, Nonlinear seismic waveform inversion in one dimension using simulated annealing: Geophysics, **56**, 1119–1122, doi: https://doi.org/10.1190/1.1889926.

Sheriff, R. E., and L. P. Geldart, 1995, Exploration seismology: Cambridge University Press.

Tromp, J., C. Tape, and Q. Liu, 2005, Seismic tomography, adjoint methods, time reversal and banana-doughnut kernels: Geophysical Journal International, **160**, 195–216, doi: –https://doi.org/10.1111/j.1365–246X.2004.02453.x.

Wang, W., G. A. McMechan, C. Tang, and F. Xie, 2016, Up/down and P/S decompositions of elastic wavefields using complex seismic traces with applications to calculating Poynting vectors and angle-domain common-image gathers from reverse time migrations: Geophysics, **81**, S181–S194, doi: –https://doi.org/10.1190/geo2015–0456.1.